Optical Fiber Technology 75 (2023) 103176

Contents lists available at ScienceDirect

Optical Fiber Technology

journal homepage: www.elsevier.com/locate/yofte

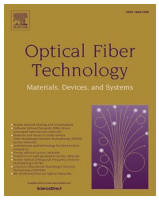

Analysis of crosstalk effects in phase-OTDR system using fiber Bragg grating array

Ertunga B. Kocal [a], Marc Wuilpart [b], Kivilcim Yüksel [a,*]

[a] Izmir Institute of Technology, Electronics Engineering Department, 35430 Urla, İzmir, Turkey
[b] University of Mons, Boulevard Dolez 31, 7000 Mons, Belgium

ARTICLE INFO

Keywords:
Phase-OTDR
Multi-reflection crosstalk
Spectral-shadowing crosstalk
FBG
Fiber optic sensor

ABSTRACT

In this paper, the parasitic components (i.e., multi-reflections, Rayleigh scattering, photodetector noise, and phase variations due to external perturbations) are analysed and based on this analysis, a new signal to noise ratio (SNR) definition is provided suitable for the FBG-assisted Phase-OTDR system. A detailed analysis of performance parameters in the presence of multi reflection crosstalk (including its first- and second-order components) and spectral shadowing crosstalk is presented. SNR was calculated for different reflectivity and spacing lengths showing that the maximum number of cascaded FBGs can be significantly increased by using lower FBG reflectivity. It was also observed that the spacing length distance does not have a significant impact on the maximum number of FBGs that can be interrogated. By comparing single-pulse and double-pulse configurations, the use of double pulse was shown to provide higher SNR values when the number of FBGs is around 100 FBGs. The multi-reflection crosstalk when combined with the spectral-shadowing effect was demonstrated to create secondary crosstalk components making the interpretation of spectral analysis more difficult.

1. Introduction

Distributed optical fiber sensing (DOFS) was developed more than 20 years ago as a powerful group of alternative technologies to conventional sensors and since then, they acquired great interest due to their advantages in terms of implementation of many successful applications [1]. Large variety of sectors have been benefiting from DOFS: including oil & gas (i.e., well and pipeline monitoring), manufacturing, energy, transportation, aerospace, security, and medicine [2]. As an example of the application areas, a review of optical fiber sensing for marine environment and marine structural health monitoring is provided in [3]. Distributed optical fiber sensing sensors make use of the intrinsic scattering mechanisms (i.e., Raman, Brillouin, and Rayleigh phenomena) in fibers, hence benefitting from all the advantages of optical fiber technology (low-weight, small dimensions and immunity to electromagnetic interference). Distributed acoustic sensing (DAS, also known as distributed vibration sensing, DVS) is the dominant application area for Rayleigh backscattering (RBS) based sensing. This sensor family relies on the fact that the intensity and/or phase of the Rayleigh backscattered light vary in response to external perturbations (through strain-optic effect). Most of the interrogation units of DAS/DVS implement variants of Phase-sensitive Optical Time Domain Reflectometry (Phase-OTDR) in which, coherent optical pulses (or pulse pairs in double-pulse configuration) are launched into the sensing fiber to perform spatially-resolved measurements of RBS [4]. Phase-OTDR has been demonstrated to reach long distances (up to hundred km), while keeping the ability of detecting high frequency variations in RBS amplitude or phase (~a few kHz) [5]. Low noise and long-range capabilities have been demonstrated in [6] by implementing linearly frequency modulated pulses and coherent detection. Even though the measurement technology itself is well understood and developed, it still remains a significant challenge to make sense of the enormous amount of data measured by sensors and to transform it into real-time process indicators with consistent results (which can generate alarms when needed) [7]. In order to extract and classify the different types of vibration events, various methods have been proposed. Examples include, among many others, utilization of differential signals [8], deep convolutional neural networks (CNNs) [9], transfer learning and support vector machine [10].

The SNR improvement of Phase-OTDR, is still an active research area, as the RBS signal is inherently weak. Moreover, the variety of applications of different nature may require different signal processing

* Corresponding author.
E-mail address: kivilcimyuksel@iyte.edu.tr (K. Yüksel).

https://doi.org/10.1016/j.yofte.2022.103176
Received 16 October 2022; Received in revised form 18 November 2022; Accepted 23 November 2022
Available online 6 December 2022

methods in order to extract the desired information with an acceptable SNR. Recently, a novel approach brought about a new paradigm for the sensitivity improvement in DAS. Rather than enhancing the interrogator and its signal processing stages, it proposes modifying the sensing fiber itself in either a distributed [11,12] or a quasi-distributed manner [13–15].

A possible way of modifying the sensing fiber is to inscribe a weak fiber Bragg grating (FBG) array along its length. The FBGs act as reflective centers having known reflection coefficients and positions. Even though weak FBG reflectivity is low (around −40 dB), they still provide signal levels higher than RBS registered by the conventional phase-OTDR. An overview of the recent advances in FBG-assisted phase-sensitive OTDR technique is provided in [16].

In FBG-assisted Phase-OTDR systems, the positions of the FBGs are generally equally spaced over the sensing fiber, where the distance between two successive FBGs defines the spatial resolution of the sensor system. There are some complications that accompany by the use of cascaded FBGs. These issues, namely multi reflection crosstalk (MRC) and spectral shadowing crosstalk (SSC) should be taken into account to be able to determine the realistic overall performance parameters of the system. In the previous literature, MRC effect has been studied by in terms of SNR analysis to calculate the longest achievable distance [17] and the time delay in polarization maintaining fibers [18]. Another research group experimentally demonstrated the generation of spectral shadowing components and proposed a mitigation method [19,20]. These two phenomena (MRC and SSC) are interrelated in the sense that the multi-reflection signals carry the spectral features of all the FBGs encountered on their paths. Hence, rather than treating only the signal power in MRC analysis as in the previous approaches, the combined effects of MRC and SSC should be analyzed together for cascaded FBGs.

In this work, we provide a detailed analysis of performance parameters obtained FBG-assisted phase-sensitive OTDR systems in the presence of MRC, including its first- and second-order components. Then, we compare the effect of MRC for two types of probe pulse, namely, single-pulse (conventional configuration) and double-pulse (use of pulse pairs of short duration instead of single long pulse).

Differently from the previous literature [17], a new SNR definition, based on the variances of the signal of interest and noise components is used. This new definition considers trace-to-trace variations which are used to detect and identify external perturbations. The interrelated MRC and SSC effects are also demonstrated. We show by the way of simulations that in addition to the primary shadowing components due to interrogating optical pulse passing through all upstream FBGs before reaching a specific FBG pair, the multi-reflection signals also carry supplementary unwanted vibration frequency components (secondary spectral shadowing frequencies) impinged on the actual signal to be measured. To the best of our knowledge, the overall quantization of the crosstalk effects including both MRC and SSC, together with their interrelated results on the slow-time analysis is presented for the first time.

2. Theoretical background

The sensor system analysed in this work is composed of a Phase-OTDR interrogator and a sensing fiber comprising a cascade of FBGs (a set of uniform, identical, equally spaced, low-reflective fiber Bragg gratings written in a single mode fiber). The so-called “direct detection” approach of Phase-OTDR has been considered, which relies on the measurement of RBS power over time. The Phase-OTDR interrogator launches optical pulses (of width W) into the sensing fiber. Fig. 1 schematically represents the measured Phase-OTDR trace obtained from a single interrogating optical pulse propagating through an array of N gratings. This OTDR trace has a comb-like characteristic comprising of interference sections ($IF_{1\&2}$, $IF_{2\&3}$, …, $IF_{(N-1)\ \&N}$) and reflection sections (FBG_1, FBG_2, …, FBG_N) [19]. These interference sections can be observed as long as the resolution cell (of width $W/2$) of the interrogator ranges from L (distance between two successive FBGs) to $2L$ (in order to not cover a third FBG). Outside the IF sections, the signal is reflected from only one FBG. Any change in path length and/or refractive index (due to an external perturbation) between two consecutive FBGs will change the phase relationship between the two corresponding reflected signals, which in turn affects the power level recorded at the OTDR within the interference zone. By performing many successive phase-OTDR traces, a dynamic analysis (or slow-time analysis) of the perturbation can be made. Let us focus on one of the interference sections, $IF_{N-1\&N}$ created by the superposition of the complex electric fields $\boldsymbol{E}_{N-1}$ and $\boldsymbol{E}_N$ (i.e., optical signals reflected from FBG_{N-1} and FBG_N). The complex reflection coefficient, $\boldsymbol{r}_N$, and the complex transmission coefficient $\boldsymbol{t}_N$ for FBG_N are determined as a function of known parameters (i.e., grating length, grating pitch, and average refractive index modulation [21]). The electric fields $\boldsymbol{E}_{N-1}$ and $\boldsymbol{E}_N$ can be represented as

$$\boldsymbol{E}_{N-1} = \boldsymbol{E}_0 \boldsymbol{T}^2(t)\boldsymbol{r}_{N-1}(t) \tag{1}$$

$$\boldsymbol{E}_N = \boldsymbol{E}_0 \boldsymbol{T}^2(t)\boldsymbol{t}_{N-1}^2(t)\boldsymbol{r}_N(t)\exp(-j\Delta\varphi(t)) \tag{2}$$

where $\boldsymbol{E}_0$ is the electric field at the Fiber Under Test (FUT) input, $\boldsymbol{T}(t)$ denotes the complex transmission coefficient of the FUT between its input and FBG_{N-1} and $\Delta\varphi(t)$ is twice the phase difference between two consecutive FBGs (FBG_{N-1} and FBG_N in this particular case). This phase difference stems from both the vibration (perturbation) and the fiber length between the FBGs. The term $\boldsymbol{T}(t)$ carries the spectral content of the upstream FBGs along the way of test signal [22]. The signal reflected

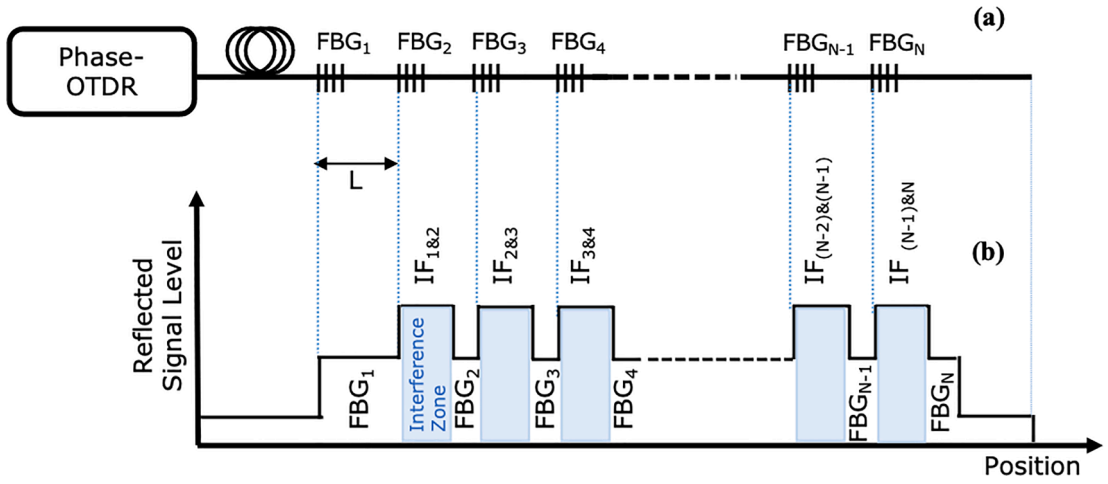

Fig. 1. (a) Sensor setup for N equally spaced FBG sensors and (b) schematic Phase-OTDR trace.

from FBG_{N-1} interferes with that of the FBG_N. Power levels corresponding to three zones (FBG_{N-1}, $IF_{N-1,\,N}$, FBG_N) shown in Fig. 1 can be respectively calculated as

$$P_{N-1} = |\boldsymbol{E}_0|^2 |\boldsymbol{T}(t)|^4 |\boldsymbol{r}_{N-1}(t)|^2 \tag{3}$$

$$P_N = |\boldsymbol{E}_{in}|^2 |\boldsymbol{T}(t)|^4 |\boldsymbol{t}_{N-1}(t)|^4 |\boldsymbol{r}_N(t)|^2 \tag{4}$$

$$P_{N-1,N} = (\boldsymbol{E}_{N-1} + \boldsymbol{E}_N)(\boldsymbol{E}_{N-1} + \boldsymbol{E}_N)^* = |\boldsymbol{T}(t)|^4 |\boldsymbol{r}_{N-1}(t)|^2 + |\boldsymbol{E}_0|^2 |\boldsymbol{T}(t)|^4 |\boldsymbol{t}_N(t)|^4 |\boldsymbol{r}_N(t)|^2 + 2|\boldsymbol{E}_0|^2 |\boldsymbol{T}(t)|^4 |\boldsymbol{t}_{N-1}(t)|^2 |\boldsymbol{r}_{N-1}(t)||\boldsymbol{r}_N(t)| \cos(\Delta\varphi(t) + \theta(t)) \tag{5}$$

where $\theta(t) = arg(\boldsymbol{r}_{N+1}(t)/\boldsymbol{r}_N(t))$. On the FUT, the vibrations can be applied either directly on an FBG or on the fiber section between the FBGs. In the former case, the reflection and transmission coefficients of the FBG is affected since $\boldsymbol{r}_N$ and $\boldsymbol{t}_N$ depends on the grating length and the average refractive index, while in the latter case, we assume the FBGs static, i.e. the vibration only leads to an axial elongation on the fiber between the FBGs (the result will be a modulation of the phase difference $\Delta\varphi(t)$ appearing in eqn.*5*). For both cases, the applied vibration has been modelled in our simulations by a periodical change of the refractive index and the axial elongation of the fiber.

3. Analysis of Multi-Reflection crosstalk (MRC)

In addition to the Phase-OTDR signature comprising the signal components given in equations (3) - (5), many possible paths of the interrogating pulse can be found which, after having been subject to multiple reflections (3 reflections, 5 reflections, …), arrive at the same time as the useful signal.

This concept is schematically represented in Fig. 2, where only one 3-reflection-path and one 5-reflection-path are represented (for $N = 8$). In this representation, the useful signal (black dashed arrow) reflects from FBG_8 having a path length of $16L$. Both 3-reflection and 5-reflection components bouncing between FBGs take a total path length of 16 L (as indicated in the last line of the path graph in Fig. 2) and reach the photodetector at the same time with the useful signal. The total number of such paths contributing to multi-reflection crosstalk signal can be calculated for 3-reflection (M_3, 1^{st} order) and 5-reflection (M_5, 2^{nd} order) cases, by equations (6) and (7), respectively.

$$M_3(N) = \sum_{i=2}^{N-1} (i-1) \tag{6}$$

$$M_5(N) = \sum_{k=1}^{N-3} \sum_{i=2}^{N-1-k} \left(ki + \sum_{j=1}^{k} (j-2)\right) \tag{7}$$

In equations (6) and (7), the useful signal is assumed to be reflected from FBG_N. M_3 (M_5) is therefore the number of crosstalk signals of 1st order (2nd order) that will be received at the Phase-OTDR detector at the same time as the signal reflected once by FBG_N. The evolution of M_3 and M_5 is given in Table 1 for various N values. One can notice from Table 1 that the number of multi-reflection components get drastically higher as the number of FBGs increases.

3.1. Signal-to-noise ratio calculations

In order to study the influence of multiple reflections on the performance of the system, the total electric field that reach the photodetector at a time corresponding to a roundtrip propagation to the FBG_N is given by

$$\boldsymbol{E}_{Total,N}(t_0) = \boldsymbol{E}_{R,N}(t_0) + \boldsymbol{E}_{Ray,N}(t_0) + \sum_{i=1}^{M_3(N)} \boldsymbol{E}_{M3_i,N}(t_0) + \sum_{l=1}^{M_5(N)} \boldsymbol{E}_{M5_l,N}(t_0) \tag{8}$$

where, $\boldsymbol{E}_{R,N}$ is the reflected electric field from the FBG_N, $\boldsymbol{E}_{Ray,N}$ denotes the contribution of Rayleigh scattering. $\boldsymbol{E}_{M3_i,N}$ and $\boldsymbol{E}_{M5_l,N}$ are the expressions for the multiple reflection components that reach the photodetector together with the signal reflected by FBG_N. If we assume that all FBGs are identical, individual multiple reflection components and reflected electric field from FBG_N can be expressed with following equations.

$$\boldsymbol{E}_{R,N} = \boldsymbol{E}_0 \boldsymbol{r} \boldsymbol{t}^{2(N-1)} e^{-\alpha NL} = E_{Ref,N} \exp(j\varphi_{Ref,N}) \tag{9}$$

$$\boldsymbol{E}_{M3_i,N} = \boldsymbol{E}_0 \boldsymbol{r}^3 \boldsymbol{t}^{2(N-2)e^{-\alpha NL}} = E_{M3_i,N} \exp(j\varphi_{M3_i,N}) \tag{10}$$

$$\boldsymbol{E}_{M5_l,N} = \boldsymbol{E}_0 \boldsymbol{r}^5 \boldsymbol{t}^{2(N-3)} e^{-\alpha NL} = E_{M5_l,N} \exp(j\varphi_{M5_l,N}) \tag{11}$$

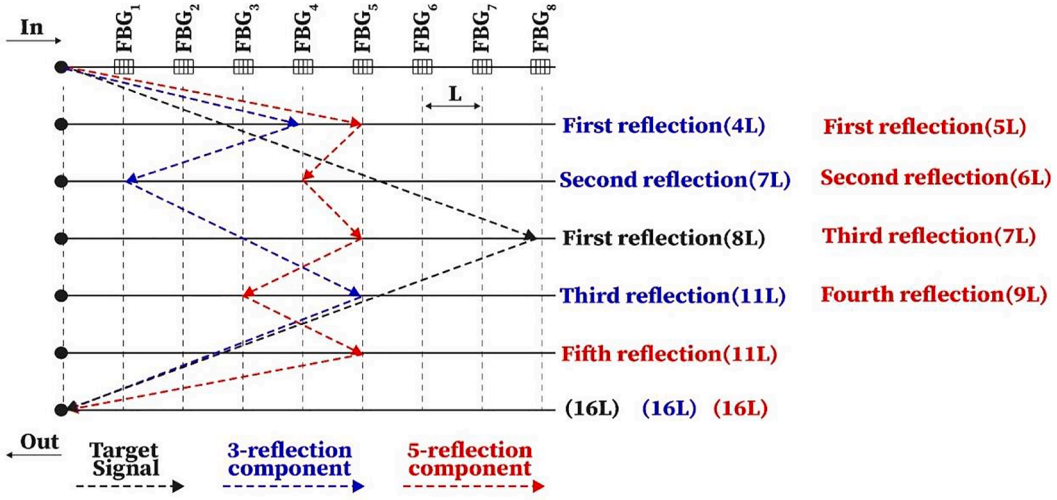

Fig. 2. Schematic representation of one example case among possible paths for 3-reflection and 5-reflection components, where the FBGs are equally spaced.

Table 1
Number of multi-reflection components for N cascaded FBGs. M_3: number of paths for 3-reflection (1st order) components. M_5: number of paths for 5-reflection (2nd order) components.

N	1	2	3	4	5	10	20	50	100	200	500	1000
M_3	0	0	1	3	6	36	171	1176	4851	19,701	124,251	498,501
M_5	0	0	0	1	6	336	8721	442,176	7,685,601	$1.2807{\cdot}10^{8}$	$5.1255{\cdot}10^{9}$	$8.2669{\cdot}10^{10}$

In equation (8), the Rayleigh scattering contribution is denoted by $\boldsymbol{E}_{Ray,N}$, whose amplitude follows a Rayleigh statistical distribution and phase is uniformly distributed over [0,2π] [23]. The mean power of Rayleigh scattering contribution can be expressed by [17]

$$P_{Ray,N} = P_0\left(1-|\boldsymbol{r}|^2\right)^{2N} v_g \tau \alpha_R S \exp(-2\alpha NL) \tag{12}$$

where v_g, τ, α_R, S, and R denote the group velocity, half of the pulse duration, the Rayleigh scattering coefficient, and the backscatter capture coefficient, respectively. Peak power of the pulse at the FUT input is denoted by P_0. In our simulation, the amplitude $\boldsymbol{E}_{Ray,N}$ is generated by using a Rayleigh distribution that provides a mean signal power value expressed by eq. (12).

It is the superposition of signals coming from two successive FBGs that is measured to detect an external perturbation applied on fiber. In eq. (13), the signal obtained from the n^{th} interference zone is expressed and the corresponding power level is denoted with eq. (14):

$$\boldsymbol{E}_{IF,n}(t_0) = \boldsymbol{E}_{Total,n}(t_0) + \boldsymbol{E}_{Total,n+1}(t_0) \tag{13}$$

$$P_{IF,n}(t_0) = \left|\boldsymbol{E}_{IF,n}(t_0)\right|^2 \tag{14}$$

In order to detect any external perturbation applied on the fiber section comprised between FBG_n and FBG_{n+1}, the time variation of the power level $P_{IF,n}$ is calculated. Axial strain is considered as an external perturbation, which causes both refractive index modification through strain-optic effect and an elongation of the sensing fiber. The difference between power levels obtained at times t_1 and t_0 is expressed by

$$\Delta P_{IF,n} = P_{IF,n}(t_1) - P_{IF,n}(t_0) \tag{15}$$

The difference in the power levels expressed with eq. (15) depends on amplitudes and phases of the electric field components contributing the total reflected signal expressed in eq. (8) (i.e., includes MRC and Rayleigh components).

The signal of interest included in equation (15) is the time variation of the interference term formed by the signals reflected by FBG_n and FBG_{n+1}. Here, the interference signal ($\Delta P_{R,n\&n+1}$) is calculated by considering only the first term of the electric field in equation (8) and is expressed by

$$\Delta P_{R,n\&n+1} = \left|E_{R,n}(t_1) + E_{R,n+1}(t_1)\right|^2 - \left|E_{R,n}(t_0) + E_{R,n+1}(t_0)\right|^2 \tag{16}$$

If we assume that the amplitudes of the reflected signal and the multiple reflection components do not change between time instants t_0 and t_1, which means that the FBGs are not affected by any external perturbation (e.g., stress, temperature variations, etc.), the difference in the interference between power levels arises from variations in phase terms of the fibers between FBGs (due to perturbations) and the amplitude/phase of the Rayleigh backscattering contribution. As it is not possible to predict exact changes in the phase terms between time instants t_0 and t_1 due to external effects (stress, temperature variations, etc.) on the fiber under test, the phases of contributors are assumed to be independent and distributed uniformly over $[0, 2\pi]$ at both t_0 and t_1. Based on this approach, the variance of the signal of interest and the noise terms at n^{th} interference zone are expressed with equations (17) and (18), respectively.

$$\sigma_S^2[n] = Var(\Delta P_{R,n\&n+1}) \tag{17}$$

$$\sigma_N^2[n] = Var\left(\Delta P_{IF,n}\right) - \sigma_S^2[n] \tag{18}$$

In equation (18), $\sigma_S^2[n]$ is subtracted from $Var\left(\Delta P_{IF,n}\right)$ as the latter includes the variation in signal of interest and all other contributors, which are independent. By using equations (17) and (18), a SNR definition is formulated by

$$SNR[n] = \frac{\sigma_S^2[n]}{\sigma_N^2[n] + \sigma_{PD}^2} \tag{19}$$

where σ_{PD}^2 denotes the variance of photodetector noise (calculated based on the noise equivalent power of a photodetector used in a typical Phase-OTDR set-up).

The simulation procedure used to determine the SNR includes the following steps: the total electric field (including the useful signal reflected from the FBG_n and the corresponding 3-reflection and 5-reflection components) is calculated by eq. (8) for all the FBGs in the array. Then, the FBGs are proceeded as pairs, where for each of them, the power of the interference zone is calculated by eq. (13) and (14). By running Monte-Carlo simulations (10 million samples are generated), variance values are determined based on equations (17)-(18). Finally, eq. (19) is used to calculate the SNR value.

3.2. Comparison of SNR with different reflectivity values

Some simulations were performed in order to investigate the effect of the FBG reflectivity on the SNR analysis. Three different reflectivity levels were considered (R = −30 dB, R = −35 dB, and R = −40 dB). It should be noted that the reflectivity value in eq. (12) is in linear scale, that is $R = 10log|\boldsymbol{r}|$. For each simulation, the FBGs placed along the sensing fiber have identical reflectivity values and a distance of 5 m is used between them. The calculated SNR as a function of interreference zone of interest is shown in Fig. 3 for different values of R ($R = -30$ dB, $R = -35$ dB, and $R = -40$ dB). The parameters τ,α, α_R, S, $\boldsymbol{E}_0$ and σ_{PD}^2 are 70 ns, 0.2 dB/km (0.046 km^{-1}), 0.032 km^{-1}, 10^{-3}, 0.1 and $3.2{*}10^{-17}$ respectively (these particular values have been selected from the most common values in the sensor applications reported in the scientific literature [17,24,25]).

Depending on the R, the maximum number of FBGs that can be interrogated before reaching a pre-determined SNR threshold changes (SNR = 10 for instance, represented in Fig. 3 by a dashed line). Even though obtained SNR values from earlier FBGs are larger with higher FBG reflectivity, the number of FBGs that can be interrogated increases drastically with lower FBG reflectivity (around 2000 with R = −40 dB). The acceptable number of FBGs and the corresponding number of IF zones (x-axis in Fig. 3) are related as represented in Fig. 1 (there exist one IF zone for each FBG pair).

The relatively higher SNR value (around 30 dB) obtained with R = −30 dB is valid only for earlier FBGs (up to 10th IF zone) and decreases rapidly down to 20 dB at around 70th IF zone. While SNR for R = −30 dB is continuously decreasing after 70th zone (and reaches the threshold at 200th IF zone), SNR = 20 dB for R = −40 dB is sustained up to 2000 FBGs.

The overall tendency is the decrease of SNR by increasing number of IF zones which is a result of combination of effects (both the decrease of useful signal level and increase of MRC components).

3.3. Effect of distance between successive FBGs

Extending the measurement range could be of crucial importance for

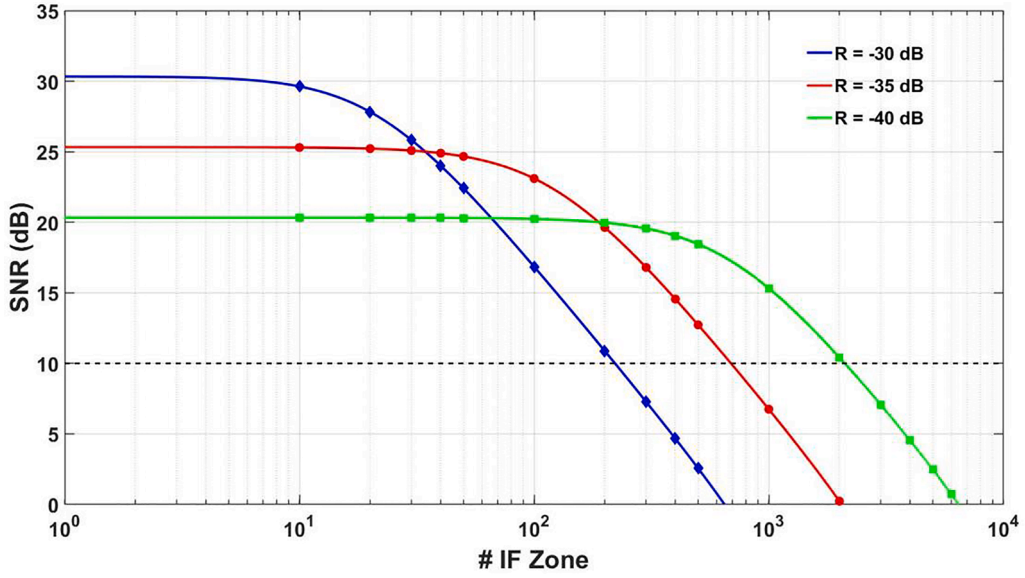

Fig. 3. SNR vs number of FBGs in the sensing fiber for 3 different reflectivity values (with MRC components).

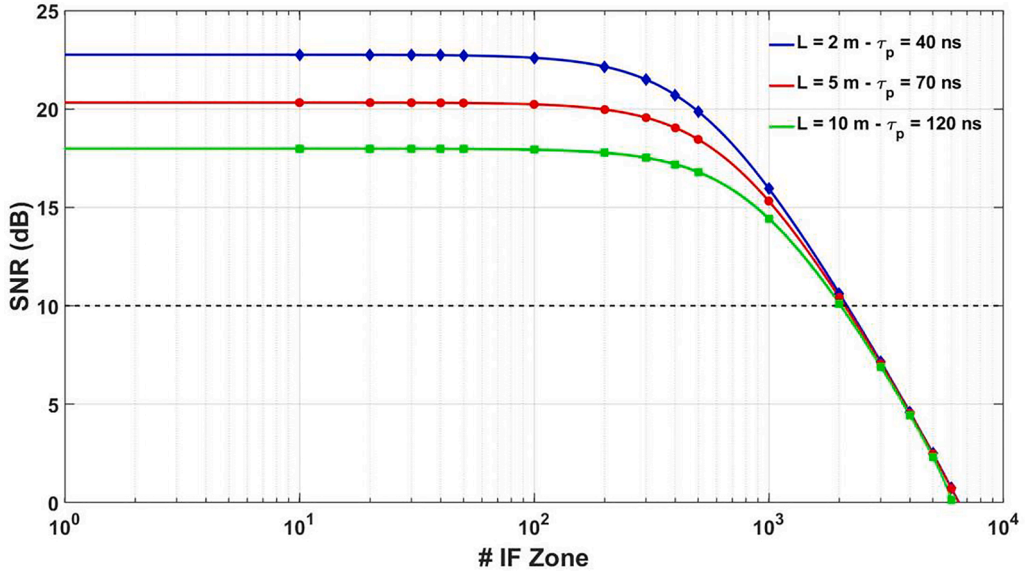

Fig. 4. SNR vs number of FBGs in the sensing fiber for 4 different L values.

some distributed vibration sensing applications. This can be achieved by increasing the distance between adjacent FBGs with the drawback to worsen the spatial resolution of the system. Some simulations were performed in order to observe the effect of increasing L (spacing length) on the SNR. An FBG reflectivity R equals -30 dB was chosen. The pulse duration is tuned (widened) depending on L to cover the distance between the successive FBGs and to ensure equal interference zone length is obtained for each case (2 m).

The SNR graphs as a function of IF zone number is represented in Fig. 4 for three different spacing lengths. For typical spacing lengths (from 2 to 10 m) the calculated SNR the first IF zones ranges from 17 dB to 23 dB. At around the 500th interference zone, the SNR curves for all spacing lengths start to converge and go into a drastic decrease. The number of FBGs that can be interrogated is 2000 for all lengths ($L = 2$ m, $L = 5$ m, and $L = 10$ m).

As shown in Fig. 4, the SNR values get lower for longer spacing length. When the spacing length increases, the Rayleigh scattering contribution gets indeed higher since the pulse duration is extended. Due to the random nature of Rayleigh scattering, increasing contribution from $P_{Ray,N}$ causes higher trace-to-trace variation within an interference zone. The results also show that after around 1000 FBGs, the calculated SNR shows little deviation and the maximum number of FBGs that can be interrogated simultaneously is almost the same for the different spacing lengths. Based on this observation, we can conclude that the MRC (which increases for the IF zone of interest) becomes the dominant restricting parasitic contributor compared to the Rayleigh noise regarding the maximum number of FBGs that can be interrogated. This leads to similar noise levels regardless of the spacing length. Therefore, spacing length distance does not have a significant impact on the maximum number of FBGs that can be interrogated.

3.4. Double short pulses vs Single long pulse

Using pulse pairs of short duration (double pulse approach) instead

of single long pulse has been proposed in the literature as a way of decreasing E_{Ray} contribution and increasing average SNR [17]. In this approach, the Rayleigh backscattered signal coming from the whole fiber section between FBGs is avoided.

The double pulse scheme was also simulated, and the results were compared with those obtained for the single pulse case. In the double pulse scheme, differently from the single pulse case, two short pulses were generated and the signals obtained from each one added to get a total signal. For the double pulse case, the total duration of the pulse pair (twice the duration of a pulse) is shorter than the duration of the pulse used in single pulse case. As a consequence, the Rayleigh scattering contribution is lower as shown by equation (12). The results are represented in Fig. 5 for two scenarios. In the first one, L is 5 m and the FBG array is interrogated using both the single pulse (τ = 70 ns) and the double pulse (τ = 20 ns) approaches. In the second simulation, L is increased to 10 m and the τ was extended to $\tau = 150$ ns and $\tau = 50$ ns for the single and double approaches, respectively. As expected, the use of a double pulse provides higher SNR values (increase of 3 dB and 5 dB in the first and second simulation, respectively) when the number of FBGs is low. The results represented in Fig. 6 also show that after around 1000 FBGs, the calculated SNR shows little deviation and the maximum number of FBGs that can be interrogated simultaneously is almost the same for both single- and double pulse configurations.

4. Multi-reflection crosstalk as a carrier of spectral shadowing

When the slow-time spectral analysis is realized on a given interference zone of the Phase-OTDR trace and considering only one round-trip of the probe signal (no MRC), the spectral shadowing components (SSCs) will appear on the spectrum [19] in addition to the frequency content really applied on the analyzed zone. We will call them as *"primary crosstalk components"*.

When the SSCs are carried by a single round-trip of the test signal, post-detection signal processing can be used to compensate them to a certain extent, as proposed in [19]. However, multi-reflection signals passing through FBGs which are subject to external perturbations result in additional SSCs (*secondary crosstalk components*). For example, suppose that three vibration signals of frequencies f_1, f_2, and f_3 are respectively applied between 1st − 2nd, 3rd − 4th, and 7th − 8th FBGs in the schematic representation of Fig. 2. When performing a frequency analysis of the power recorded in IF zone # 7 (between FBG_7 and FBG_8), additional unwanted frequency components will appear. The frequency f_3 will be detected as expected but the addition of the 3-reflection MRC components (the blue dashed line in Fig. 2 shows an example), which are subject to the first two vibration sources and carry their spectral content (f_1, f_2), will induce additional detected frequencies that are not physically generated between FBG_7 and FBG_8. Hence, the determination of a straightforward analytical formula to eliminate these components as shown in [19] is difficult to achieve.

It can be easily shown that, secondary crosstalk components include not only the original vibration frequencies but also some supplementary terms of summation and subtraction between them. Revisiting our previous example, the interference between the useful signal and the 3-reflection component represented in Fig. 2 results in the frequency components such as f_3-f_1, f_3-f_2, $f_3 + f_2$, $f_3 + f_1$ and so on (much more frequency components can be listed by taking other MRC components (that are not represented in Fig. 2) into consideration. This phenomenon may result in a misjudgment on the presence of an event on a particular location.

In order to demonstrate the combined effect of MRC and SSC, simulations were performed for various test scenarios. The electric field of MRC components have been added to the simulation procedure by tracking all the possible 3-reflection paths followed by the probe signal. The contribution of Rayleigh scattering is also considered as before. The amplitudes and phases of all contributors (useful signal, 3-reflection components, Rayleigh scattering) are calculated separately.

An example test case for 51 identical FBGs (50 IF zones) having $|\mathbf{r}|$ = ~0.01 % of reflectivity (R = -40 dB) is represented in Fig. 6. The spacing between the FBGs was set to 4 m and 10 m-long optical pulses were simulated to obtain interference between signals coming from successive FBGs.

3 vibrations were applied on sections between FBG pairs affecting the closest FBGs on both sides (i.e., FBG_N and FBG_{N+1} for N^{th} interference zone). Vibrations were applied on sections between 1st and 2nd, 24th-25th and 48th-49th FBGs with frequencies 500 Hz, 700 Hz and 2000 Hz, respectively. The axial maximum strain amplitude applied by the vibrations was selected in accordance with the previous literature [22] as 0.1 με. The corresponding maximum refractive index changes is equal to 3.15 10^{-8}.

In the scenario, both change in FBG reflection coefficient and elongation of perturbed fiber section were simulated. The configuration was chosen such that it was possible to observe/evaluate both primary and secondary SSC components. For instance, MRC components that are subject to vibration-1 and vibration-2 carry their spectral content (500

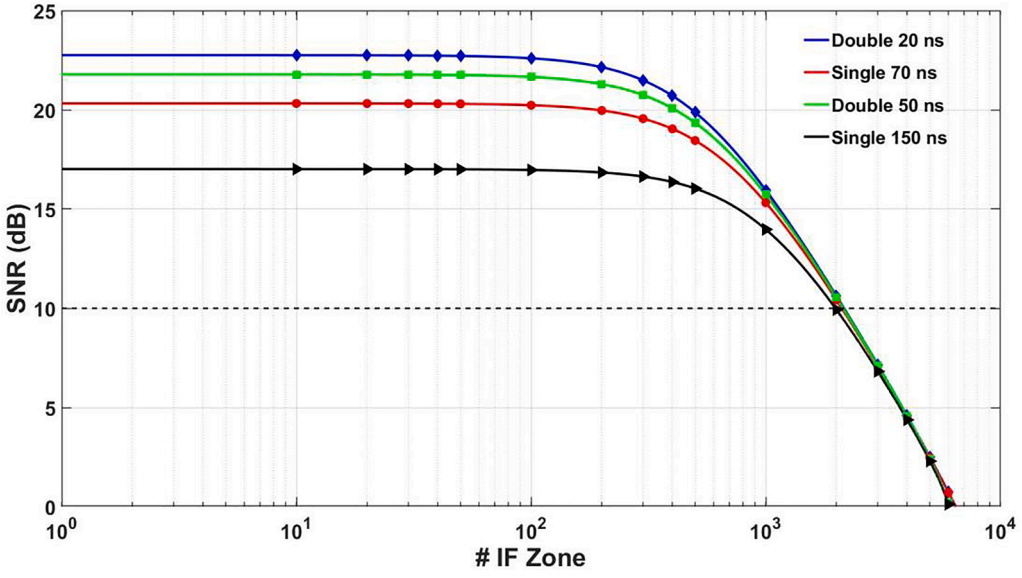

Fig. 5. Comparison of double-pulse and single pulse schemes.

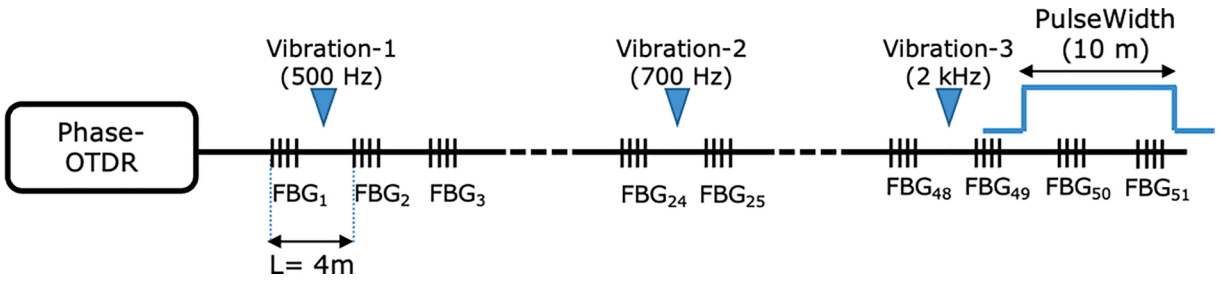

Fig. 6. Schematic representation of one example scenario.

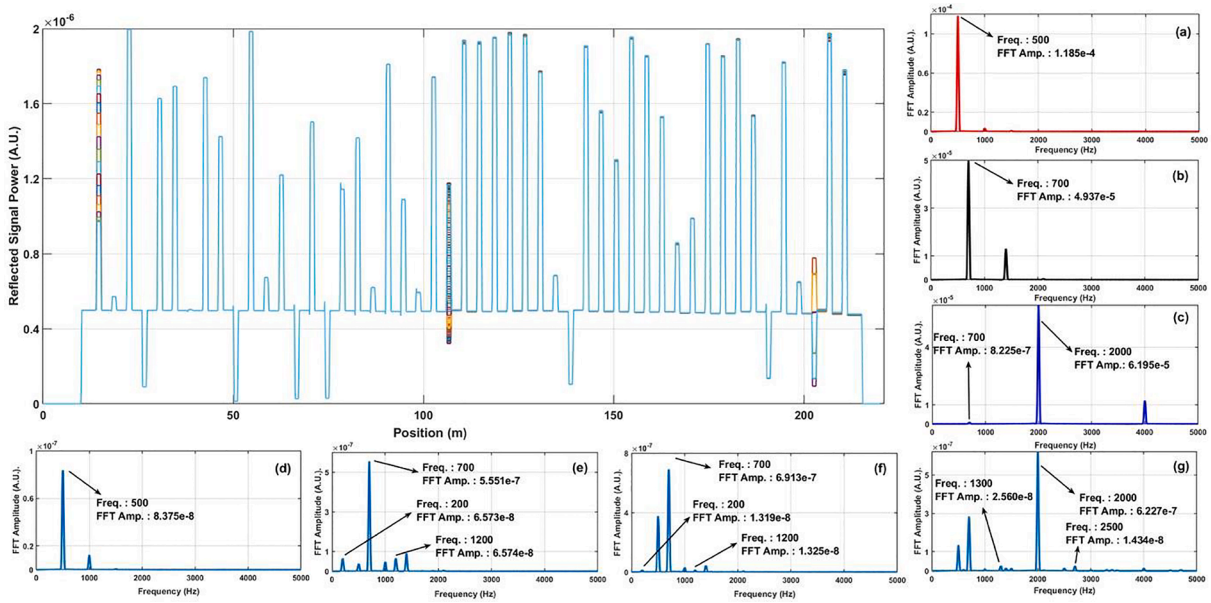

Fig. 7. Reflected signal power versus position over time. Sub-figures (a), (b), (c), (d), (e), (f), (g) show the frequency content of IF zones #1, #24, #48, #15, #30, #45 and #50, respectively.

Hz and 700 Hz) into other IF zones (cf. Fig. 7). Moreover, additional frequency components will appear stemming from the interference between the useful signal and the MRC components (2 kHz − 700 Hz, 2 kHz − 500 Hz, 2 kHz + 700 Hz, 2 kHz + 500 Hz, and so on). We considered only the 3-reflection components.

In Fig. 7, the simulated Phase-OTDR trace obtained versus time are superposed. This comb-like signature consists of reflections from FBGs, interference zones between neighboring reflections, and random RBS. The figure shows the reflected power from 51 FBGs resulting in 50 interference zones. The peak powers recorded in interference zones show variations because of the vibrations applied along the sensing fiber. Sub-figures (a), (b) and (c) show the frequency content of the power variations recorded in IF zones #1, #24, and #48, respectively i.e., where the vibrations are applied.

The frequencies 500 Hz, 700 Hz and 2000 Hz can be easily observed as expected (harmonics are also observed in these graphs at 1 kHz, 1.4 kHz, and 4 kHz, respectively). The MRC components are not distinguishable here because of the low reflectivity of the gratings (R = -40 dB).

Slow-time spectral analysis obtained in the interference zones #15, #30, #45 and #50 are presented in sub-figures (d), (e), (f) and (g), respectively. In sub-figures (e) and (f), we can observe both *"primary crosstalk components"* (500 Hz & 700 Hz) and *"secondary crosstalk components"* (700 −500 = 200 Hz & 700 + 500 = 1200). At interference zone #50, which is after all perturbed FBGs, spectral shadowing caused by all vibration events can be easily distinguished as shown in sub-figure (g). In this case, secondary crosstalk components are formed by interference between 3 primary crosstalk components (500 Hz, 700 Hz & 2000 Hz).

The amplitudes of crosstalk components in the frequency domain for a given position, depend on relative phases of all reflected electric fields adding up at that position. We expect that applied vibrations on upstream FBGs will generate crosstalk components with higher amplitudes in IF zones located further on the Phase-OTDR trace as the number of MRC components (given in Table 1) is increased. In order to verify this hypothesis, the same configuration was simulated 1000 times and the spectral slow-time analysis was conducted at each interference zone. The 1000 amplitudes of SSC component at 500 Hz (vibration applied on section between the first and the second FBGs) were calculated at each interference zone and averaged.

In Fig. 8, the averaged amplitude of crosstalk component at 500 Hz frequency is shown. As expected, relative amplitude of crosstalk components get higher as the measurement location gets further away. The reason behind this phenomenon is that with increasing number of FBGs, total count of multiple reflection components accompanying the target signal increases and the accumulated crosstalk component amplitudes become higher. These results show that if a configuration comprising hundreds of FBGs is used, multiple reflection crosstalk induces gradually increasing noise to the system and can cause fault in detection of vibration events.

Using a random distribution of the distances between the FBGs can be proposed to effectively mitigate the multi-reflection crosstalk and its consequences.

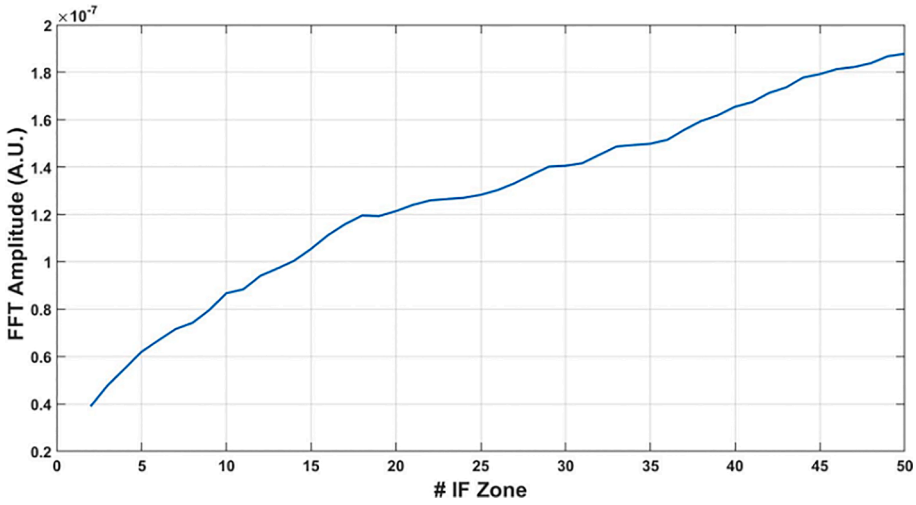

Fig. 8. Reflected signal power versus position over time at 500 Hz.

5. Conclusion

An SNR definition based on the variance of the signal of interest (interference of reflected signals from adjacent FBGs) and parasitic components (multi-reflections, Rayleigh backscattering, photodetector noise, phase variations) was proposed and its value for different FBG reflectivity and spacing lengths were presented.

The results showed that the SNR values obtained with higher FBG reflection coefficients are larger for the first interference zone, whereas the maximum number of cascaded FBGs can be significantly increased by using lower FBG reflectivity.

It was also observed that the spacing length distance does not have a significant impact on the maximum number of FBGs that can be interrogated. This can be explained by the fact that Rayleigh contribution to the noise becomes negligible compared to MRC, which leads to similar noise levels regardless of the spacing length. The single-pulse and double-pulse configurations were also compared. The use of double pulse has been shown to provide higher SNR values when the number of FBGs is low (around 100 FBGs).

Multi-reflection and spectral-shadowing crosstalk effects have been studied by the way of simulations. The presence of "*primary crosstalk components*" and "*secondary crosstalk components*" at interference zones for a perturbed fiber is demonstrated. Increase in the relative amplitude of crosstalk components shows that SSC and MRC become more disturbing with increasing the sensing range for configuration comprising equally spaced FBGs. These results indicate the importance of multi-reflection crosstalk and spectral shadowing crosstalk as restrictive noise components in calculations of sensing distance limits.

Declaration of Competing Interest

The authors declare that they have no known competing financial interests or personal relationships that could have appeared to influence the work reported in this paper.

Data availability

The data that has been used is confidential.

References

[1] B.G. Gorshkov, K. Yüksel, A.A. Fotiadi, M. Wuilpat, D.A. Korobko, A.A. Zhirnov, Scientific Applications of Distributed Acoustic Sensing: State-of-the-Art Review and Perspective, Sensors 22 (3) (2022) 1033.
[2] A. Hartog, in: G.T.V. Grattan, B.T. Meggitt (Eds.), Optical fiber sensor technology, Kluwer Academic Publishers, 2000.
[3] R. Min, Z. Liu, L. Pereira, C. Yang, Q. Sui, C. Marques, Optical fiber sensing for marine environment and marine structural health monitoring: A review, Opt. Laser Technol. 140 (2021), 107082.
[4] R. Juskaitis, A.M. Mamedov, V.T. Potapov, S.V. Shatalin, Interferometry with Rayleigh backscattering in a single-mode optical fiber, Opt. Lett. 19 (3) (1994) 225–227.
[5] F. Uyar, T. Onat, C. Unal, T. Kartaloglu, E. Ozbay, I. Ozdur, A Direct Detection Fiber Optic Distributed Acoustic Sensor with a Mean SNR of 7.3 dB at 102.7 km, IEEE Photonics J. 11 (2019).
[6] O.H. Waagaard, E. Rønnekleiv, A. Haukanes, F. Stabo-Eeg, D. Thingbø, S. Forbord, S.E. Aasen, J. Kristoffer Brenne, Real-time low noise distributed acoustic sensing in 171 km low loss fiber, OSA, Continuum 4 (2021) 688–701.
[7] : C. E. Kayan, K. Yuksel Aldogan, A.Gumus, An Intensity and Phase Stacked Analysis of Phase-OTDR System using Deep Transfer Learning and Recurrent Neural Networks, arXiv:2206.12484v2 [cs.LG], https://doi.org/10.48550/arXiv.2206.12484.
[8] M. Adeel, C. Shang, D. Hu, H. Wu, K. Zhu, A. Raza, C. Lu, Impact-Based Feature Extraction Utilizing Differential Signals of Phase-Sensitive OTDR, J. Lightwave Technol. 38 (8) (2020) 2539–2546.
[9] H. Wu, B. Zhou, K. Zhu, C. Shang, H. Yaw Tam, C. Lu, Pattern recognition in distributed fiber-optic acoustic sensor using an intensity and phase stacked convolutional neural network with data augmentation, Opt. Express 29 (2021) 3269–3283.
[10] Y. Li, X. Zeng, Y. Shi, Quickly build a high-precision classifier for Φ-OTDR sensing system based on transfer learning and support vector machine, Opt. Fiber Technol. 70 (2022), 102868.
[11] S. Loranger, M. Gagné, V. Lambin-Iezzi, R. Kashyap, Rayleigh scatter-based order of magnitude increase in distributed temperature and strain sensing by simple UV exposure of optical fibre, Sci. Rep. 5 (2015) 11177.
[12] G. Cedilnik, G. Lees, P.E. Schmidt, S. Herstrøm, T. Geisler, Pushing the Reach of Fiber Distributed Acoustic Sensing to 125 km without the Use of Amplification, IEEE Sens. Lett. 3 (2019) 1–4.
[13] A. Donko, R. Sandoghchi, A. Masoudi, M. Beresna, G. Brambilla, Low-Loss Micro-Machined Fiber with Rayleigh Backscattering Enhanced By Two Orders Of Magnitude. In Proc. of the 26th Int. Conference on Optical Fiber Sensors, Lausanne, Switzerland, 24–28 September 2018.
[14] Y. Shan, W. Ji, X. Dong, L. Cao, M. Zabihi, Q. Wang, Y. Zhang, X. Zhang, An enhanced distributed acoustic sensor based on UWFBG and self-heterodyne detection, J. Lightwave Technol. 37 (2019) 2700–2705.
[15] K. V. Stepanov, A. A. Zhirnov, A. O. Chernutsky, K. I. Koshelev, A. B. Pnev,A. I. Lopunov, O. V. Butov, The Sensitivity Improvement Characterization of Distributed Strain Sensors Due to Weak Fiber Bragg Gratings, Sensors 20, (2020) 6431; doi: 10.3390/s20226431.
[16] K. Yüksel, J. Jason, E. B. Kocal, M. L. -A. Sainz and M. Wuilpart, An Overview of the Recent Advances in FBG-Assisted Phase-Sensitive OTDR Technique and its Applications, 2020 22nd International Conference on Transparent Optical Networks (ICTON), 2020, pp. 1-7, doi: 10.1109/ICTON51198.2020.9203322.
[17] T. Liu, F. Wang, Q. Yuan, Y, Liu, L. Zhang, X. Zhang, Simulation of the performance of Phase-Sensitive OTDR Based on Ultra-weak FBG Array using Double Pulse, 16th International Conference on Optical Communications and Networks, doi: 10.1109/ICOCN.2017.8121294 (2017).
[18] Y. Zheng, H. Yu, H. Guo, X. Li, D. Jiang, "Theoretical calculations of crosstalk and time delay in identical FBG array in PM fiber, IEEE Sensors (2016) 1–3, https://doi.org/10.1109/ICSENS.2016.7808476.
[19] V. de Miguel Soto, J. Jason, D. Kurtoglu, M. Lopez-Amo, M. Wuilpart, Spectral shadowing suppression technique in phase-OTDR sensing based on weak fiber Bragg grating array, Opt. Lett. 44 (2019) 526–529.

[20] F. Sandah, M. Dossou, M. Wuilpart, Spectral Shadowing Compensation in Double-pulse FBG-assisted φ-OTDR, Photon. Electromagnet. Res. Sympos. (PIERS) (2022) 530–535.
[21] T. Erdogan, Fiber Grating Spectra, J. Lightwave Technol. 15 (1997) 1277–1294.
[22] K. Yüksel, P. Megret, V. Moeyaert, M. Wuilpart, Complete Analysis of Multireflection and Spectral Shadowing Crosstalks in a Quasi- Distributed Fiber Sensor Interrogated by OFDR, IEEE Sens. J. 12 (2012) 988–995.
[23] J. Goodman, Statistical properties of laser speckle patterns, Laser Speckle and Related Phenomena 9 (1963) 57.
[24] L.B. Liokumovich, N.A. Ushakov, O.I. Kotov, M.A. Bisyarin, A.H. Hartog, Fundamentals of Optical Fiber Sensing Schemes Based on Coherent Optical Time Domain Reflectometry: Signal Model Under Static Fiber Conditions, J. Lightwave Technol. 33 (17) (2015) 3660–3671, https://doi.org/10.1109/JLT.2015.2449085.
[25] A. Bertholds, R. Dandliker, Deformation of single-mode optical fibers under static longitudinal stress, J. Lightwave Technol. 5 (7) (1987) 895–900.